

Short mode-locked pulses from planarized Y-coupled THz lasers

U. Senica,^{1, 2, a)} T. Bühler,^{1, 3} S. Cibella,⁴ G. Torrioli,⁴ M. Beck,¹ J. Faist,¹ and G. Scalari^{1, b)}

¹⁾*Quantum Optoelectronics Group, Institute of Quantum Electronics, ETH Zürich, 8093 Zürich, Switzerland*

²⁾*John A. Paulson School of Engineering and Applied Sciences, Harvard University, 02138 Cambridge, USA*

³⁾*Institute of Physics and Center for Quantum Science and Engineering, Ecole Polytechnique Fédérale de Lausanne, CH-1015 Lausanne, Switzerland*

⁴⁾*Istituto di Fotonica e Nanotecnologie, CNR, Via del Fosso del Cavaliere 100, 00133 Rome, Italy*

(Dated: 10 February 2026)

Short THz pulses are highly attractive both for fundamental research and practical applications in this underdeveloped region of the electromagnetic spectrum. Typically, THz pulses are generated using nonlinear optical methods, starting from a high-power visible or near-IR mode-locked source, but usually suffer from low conversion efficiencies. Here, we present a direct on-chip THz source of coherent short pulse trains based on active mode-locking of an inverse-designed planarized Y-coupled THz quantum cascade laser. By employing quasi-resonant microwave modulation of the asymmetric laser cavity, mode-locked pulses as short as 2.3 ps are generated, with emission bandwidths spanning 500 and 700 GHz at a central frequency of 2.9 THz.

I. INTRODUCTION

Short THz pulses are important both for fundamental studies and for applications. In solid-state systems, THz excitations allow to access a variety of phenomena, driving the system out of equilibrium and reaching new phases^{1,2}. In this case, THz pulses with large field amplitudes (>100 kV/cm) are needed. In several applications, especially for non-destructive material inspection³ and linear spectroscopy, the requirements on the field amplitude are less extreme and table-top sources based on femtosecond lasers are routinely employed⁴. Such time-domain sources typically rely on photoconductive antennas, ensuring large bandwidth and high dynamic range but with relatively low intensity above 1.5 THz (<50 μ W). Quantum cascade lasers (QCLs)^{5,6} have nowadays reached technological maturity and in the last decade, frequency comb operation of QCLs has progressed considerably, with the demonstration of active mode-locking⁷, self-starting FM comb operation^{8,9}, soliton formation in ring cavities¹⁰⁻¹², and fully controllable FM states¹³. THz QCLs¹⁴ constitute a powerful, compact source of THz radiation spanning the 1-6 THz frequency range^{15,16}, with recent demonstrations of thermoelectric cooler operation^{17,18}. Due to their metallic waveguides^{19,20}, they are especially suitable for broadband operation²¹ and efficient control with microwaves. THz devices have shown impressive performance as frequency combs²²⁻²⁴, covering bandwidths above 1 THz²⁰. For some applications, a stable pulse operation is necessary: active mode-locking of THz QCLs has been observed in double metal waveguides with pulse lengths down to around 4-5 ps^{20,25}.

In this paper, we demonstrate active mode-locking in an inverse-designed Y-coupled planarized waveguide configuration, reaching measured pulse lengths as short as 2.3 ps and 3.6 ps, spanning a bandwidth of 500 GHz and 700 GHz, respectively. Y-coupled quantum cascade lasers have previ-

ously been investigated both in the mid-IR²⁶ and THz spectral ranges^{27,28}, but without addressing mode locking and pulse generation.

II. LASER DEVICE STRUCTURE

Our devices are based on a high-performance planarized THz QCL platform that we recently developed²⁰. In particular, a broadband, low-threshold homogeneous quantum cascade active region²⁹ is used within the active waveguide core, and the whole structure is planarized in the low-loss polymer BCB. Instead of using standard ridge devices, we developed several Y-coupled waveguides, useful as broadband on-chip power splitters. The device layout was obtained using advanced inverse design techniques³⁰: previously, we have demonstrated the applicability of such optimization approaches in our waveguide platform by developing inverse-designed reflectors for high-power emission³¹ and, more recently, a compact active three-channel wavelength division multiplexer³². In the optimization stage, the Figure of Merit (FOM) was to maximize equal transmission into both Y-splitter waveguide arms over an octave-spanning spectrum between 2-4 THz (the resulting simulated performance is in the Supplementary Material, Fig. S1, S2).

In Fig. 1(a), we show an optical microscope image of a fabricated planarized Y-coupled device with symmetric arms. The bottom right inset shows the simulated electric field intensity at the central frequency of 3 THz, displaying minimal reflection and scattering losses. These first-generation devices consist of 20 μ m wide waveguides to minimize the laser threshold current and heating, and the two upper arms were separated by 160 μ m to prevent transversal mode coupling. The second generation of devices, shown in panel (b), features a modified Y-splitter region, where a 40 μ m wide waveguide splits into two 20 μ m wide arms, which are then expanded into 40 μ m wide ridges via a tapered section. A wider ridge width was chosen to reduce the waveguide losses and increase the emission bandwidth and output power. Additionally, asymmetric devices were fabricated, where a relative phase shift is induced between the two upper waveguide sections, either by

^{a)}usenica@seas.harvard.edu

^{b)}scalari@phys.ethz.ch

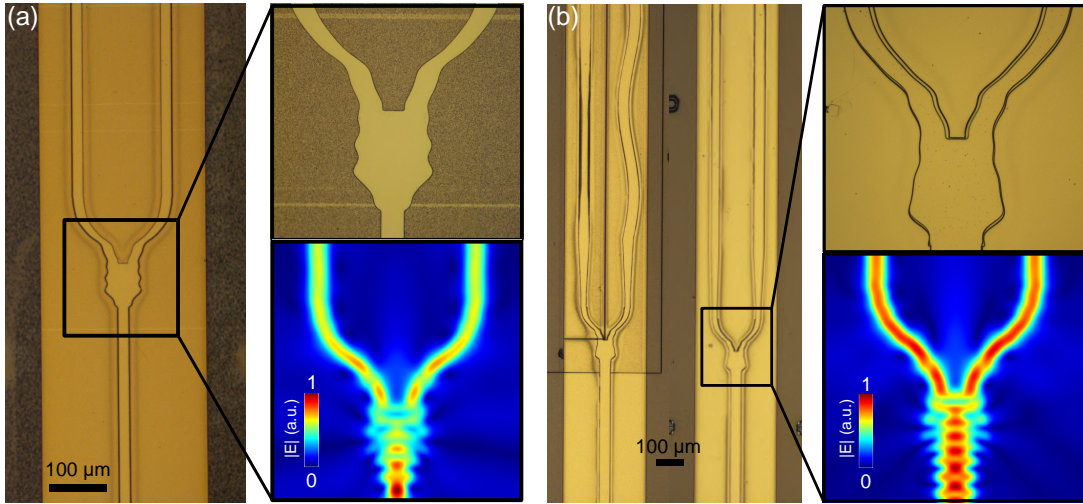


FIG. 1. Optical microscope images of two generations of planarized Y-coupled waveguides, where the splitter region was obtained using inverse design (zoomed-in region shown in the top right insets). The original symmetric design is shown in (a), while the second-generation splitter design with asymmetric arms is displayed in (b). The bottom right insets show the simulated electric field intensity at 3 THz, which is split equally into both Y-splitter arms with minimal reflections or scattering losses.

a modified length or width (effective index difference).

III. RESULTS

A. Symmetric Y-coupled device

Experimentally, we first characterized the symmetric device from Fig. 1(a). All the measurements were performed in an evacuated helium flow cryostat at stabilized heat sink temperatures of around 20 K. Due to the narrow arm widths of 20 μm , this sample features a relatively low threshold current of 60 mA (see also the LIV curve in Supplementary Material, Fig. S3). In Fig. 2(a-c), we plot the measured emission spectra for an increasing DC laser bias. For low bias voltages, an emission bandwidth of around 500 GHz and a single narrow RF beat note are measured, indicating an equidistant mode spacing characteristic for frequency comb operation (see also the RF beatnote map in Supplementary Material, Fig. S4). For higher voltages, the emission bandwidth is increased, spanning up to 1 THz bandwidth in panel (c). However, there is no single narrow RF beat note observed due to significant chromatic dispersion within the laser cavity, which limits the obtainable bandwidth of coherent comb states.

In panels (d-e), we show far-field patterns measured from the front side of the device with two arms, and each panel corresponds to the emission spectrum on the left side. In double metal waveguide THz QCLs, the far-field pattern is typically scattered across the entire range of measurement angles ($\pm 40^\circ$). In contrast, for symmetric Y-coupled devices, we see a characteristic interference pattern in the horizontal direction, with clear regions of local maxima and minima. These occur due to constructive and destructive interference between the light emitted from both waveguide arms. Such a symmetric and high-contrast pattern is an indication that the two arms

emit the same intensity and are perfectly in phase for each lasing mode in the emission spectrum, which is expected for a fully symmetric device with a 50:50 power splitting ratio. The asymmetric shape in the vertical direction occurs due to partial reflections of the emitted THz radiation from the copper submount, as this sample is mounted slightly back from the edge.

In the Supplementary Material, we present a more detailed discussion that verifies the equal power splitting and phase of the two arms, including an analytical calculation study of the predicted far-field patterns as a function of phase difference and power splitting ratio, which could potentially be employed for beam steering applications.

B. Asymmetric Y-coupled device

Measurements of asymmetric devices from Fig. 1(b) display very different results, and a single RF beatnote is measured only for very low bias currents just above threshold. In fact, as shown in the RF beat note map in Fig. 3(a), where the RF signal is recorded as a function of the applied laser bias voltage, a complex pattern in the RF signals is observed. In the bottom part of panel (b), we show the measured THz spectrum with a laser bias voltage close to 9 V (within the first region in the beatnote map from panel (a), marked with a blue dashed line). At first glance, the THz spectrum does not look particularly interesting. However, a simple peak position analysis reveals that the extracted mode spacing varies in a very broad range between 13-17 GHz, as shown in the top part of panel (b). Together with the dense RF spectrum with many lines, this indicates a complex behavior induced by the phase-shifted arms.

To investigate this, we modeled the entire asymmetric Y-coupled cavity using full-wave 3D simulations and studied

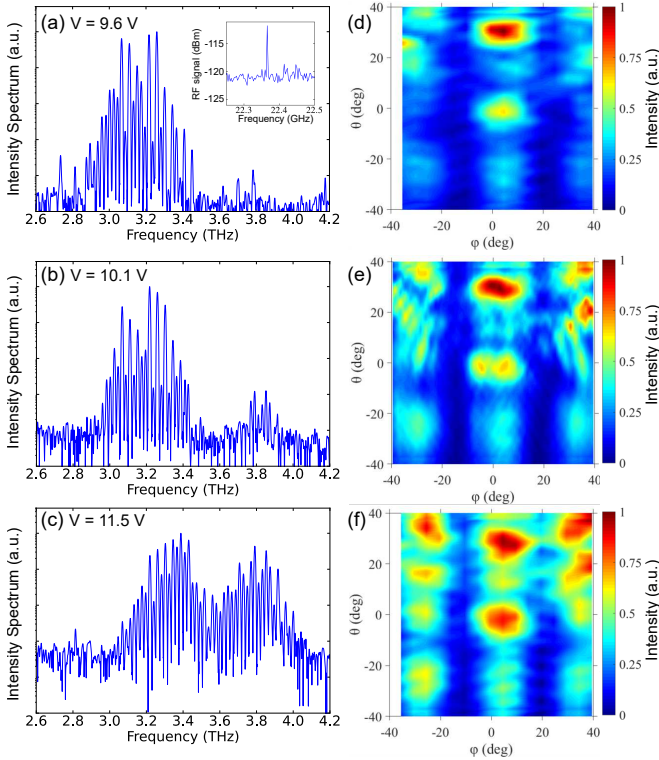


FIG. 2. Experimental emission spectrum (a-c) and corresponding far-field pattern measurements (d-f) of a symmetric Y-coupled device extracted from the side with two arms. The characteristic high-contrast symmetric interference pattern along the horizontal direction is an indication that the two arms emit equal intensities and are in phase throughout the spectrum for different laser bias points.

both its resonant modes (eigenmode analysis) as well as the spatiotemporal evolution of the intracavity electric field intensity (time-domain propagation). While more details can be found in the Supplementary Material, the main finding is that the asymmetric design with the induced phase shifts between the two arms results in a complex spectral and temporal evolution of the field. In particular, the usual regime with regular (nearly) equidistant longitudinal modes co-existing within a simple Fabry-Pérot laser is no longer a valid assumption. Instead, a quasi-continuum of modes with similar losses available for lasing exists simultaneously. In combination with spatial hole burning and asymmetric gain/amplification within the individual arms, this results in dense, yet highly irregular emission spectra. We should note that the RF spectrum, with its numerous narrow lines, suggests that there is an even larger number of lasing modes in the THz emission spectrum than what our FTIR spectrometer measurements can resolve. This behavior is somewhat similar to that of random lasers³³, where a (pseudo)random distribution of scattering elements within the laser cavity can support many different modes with unequal frequency spacing. It has to be underlined that the presence of narrow multiple beatnotes indicates coherence between modes at different roundtrips.

While this hinders the formation of free-running comb states in asymmetric devices, it also makes them very suit-

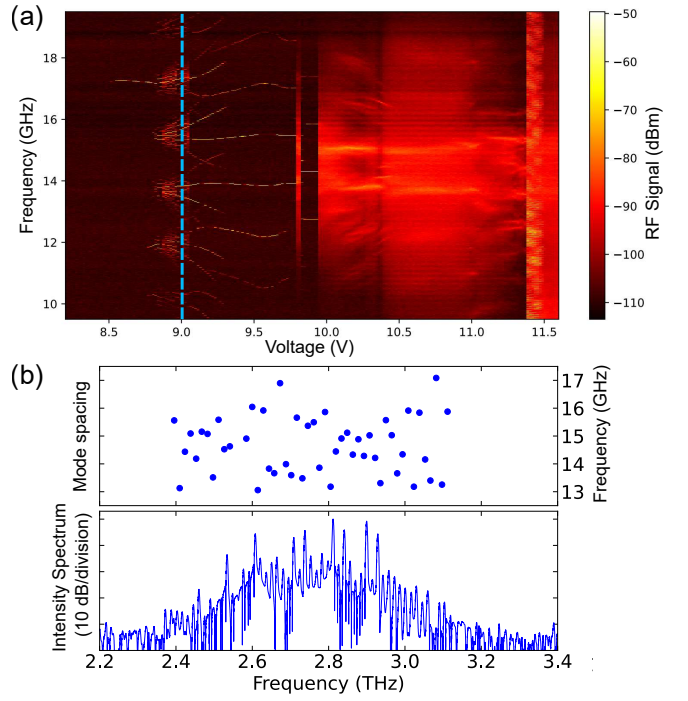


FIG. 3. (a) RF beatnote map of an asymmetric Y-split device measured in CW at 25 K. A seemingly chaotic RF signal is observed through the majority of the bias range. (b) Measured THz emission spectrum of an asymmetric Y-split device (bottom panel), which has a very irregular mode spacing. This is also evident in the extracted mode spacing (top panel) as well as in the RF spectrum, which features many lines (blue dashed line in (a)).

able for microwave modulation experiments. In particular, we can bias the laser close to the lasing threshold and modulate the cavity close to its natural repetition rate, defined as $f_{\text{rep}} = \frac{c}{2n_g L}$, where c is the speed of light in vacuum, n_g is the group index of the propagating mode, and L is the cavity length. The latter can be defined as the average propagation path of traversing the single waveguide and one of the two Y-coupled arms. In this configuration, we can generate coherent trains of short pulses via active mode-locking. These measurements were performed using SWIFT spectroscopy^{22,34}, where the optical beatnote is measured using a fast THz detector in combination with an FTIR spectrometer and an I/Q demodulator. In our case, we used a fast superconducting hot electron bolometer (HEB) detector, which can be operated above 30 GHz³⁵. In Fig. 4, we display the measured emission spectra, the intermodal phase differences, and the reconstructed time domain intensities. In panels (a-c), we show a relatively flat emission spectrum over a bandwidth of 500 GHz, where the intermodal phase differences are zero across the entire bandwidth. In the time domain, this produces a train of pulses with an FWHM width of 2.3 ps. These are the shortest mode-locked pulses from a THz QCL to date, and nearly a factor of two shorter than previous active and passive mode-locked demonstrations with pulse durations down to 4.0 ps^{20,25,36,37}. In panels (d-f), we show another mode-locked state, where the emission bandwidth spans 700 GHz

and the smooth spectral envelope is similar to those obtained in temporal solitons, typical for microresonator combs based on the Kerr nonlinearity³⁸. In the time domain, this produces very clean pulses with a reconstructed duration of 3.6 ps. Due to the limited S/N ratio and dynamic range of the HEB detector, only the strongest central modes of the emission spectrum could be measured with SWIFT spectroscopy, so the actual pulse duration is most probably significantly shorter (estimated about 2.7 ps). The nominal length of the cleaved asymmetric Y-coupled device is approximately 2.7 mm. The RF modulation frequencies were 15.68 GHz and 15.71 GHz, which would correspond to a 2.5 mm long homogeneous ridge with an active waveguide width of 40 μ m. Based on the measured detector intensity, the peak pulse power is on the order of 10 mW.

Additionally, another interesting regime can be accessed with these devices: similar to our recent work³⁹, by strongly modulating the laser cavity with an RF signal of (nearly) arbitrary frequency, emission spectra with mode spacings that precisely follow the modulation frequency can be generated. This is shown in Fig. 5(a), where broadband tunable spectra are displayed as a function of modulation frequency and mode spacing. In panel (b), we plot the extracted mode spacing of these spectra. For most of the broad range of RF modulation frequencies between 6-18 GHz, the THz spectral mode spacing indeed matches the RF modulation frequency. Correspondingly, the THz emission bandwidth is the widest in this region. This happens close to the expected free-running mode spacing of a Fabry-Pérot device of a similar length. In the Supplementary Material, we added a detailed study of the different types of states that occur throughout the RF modulation frequency sweep, along with an analytical model of the modulated laser cavity, as well as SWIFT spectroscopy results on one of the broadband states.

IV. CONCLUSIONS

In conclusion, we have presented inverse-designed Y-coupled lasers based on the planarized THz QCL platform.

Symmetric devices display characteristic interference patterns in the measured far-field distributions across the entire dynamic range of the device, with broadband incoherent emission spanning up to 1 THz. The far-field interference patterns can be attributed to the phase-locked operation of the two laser arms. In principle, one could control the phase and amplitude within the individual arms by using independent electrical contacts for the different sections. This way, the horizontal angle/direction of the output beam could be tuned, interesting for applications that require dynamic beam steering. Similar to phased array antennas, a tree array cascaded sequence of Y-coupled sections⁴⁰ could be used to further focus the central beam emission.

On the other hand, asymmetric devices display a seemingly chaotic behavior under free-running operation. This

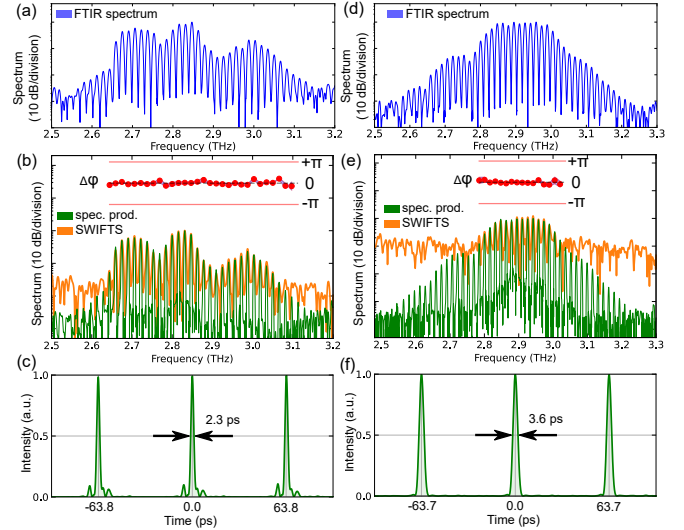


FIG. 4. Measured FTIR spectra and SWIFT spectroscopy results of actively mode-locked asymmetric Y-coupled devices. (a-c) A relatively flat spectrum over a bandwidth of 500 GHz with zero intermodal phase differences produces the shortest pulses of 2.3 ps. (d-f) An even broader emission spectrum of 700 GHz, similar in shape to a soliton spectral envelope, produces very clean pulses with a duration of 3.6 ps. The actual pulse duration is most likely even shorter (2.7 ps), as only the central part of the spectrum could be measured with SWIFTS.

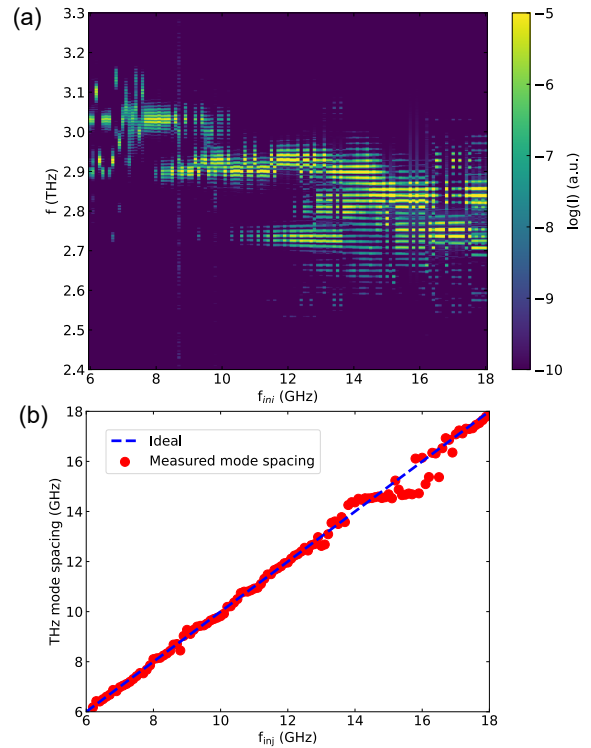


FIG. 5. Experimental sweep of the RF modulation frequency with (a) the corresponding THz emission spectra and (b) extracted mode spacing.

can be explained by the induced phase shift between the two Y-coupled arms, giving rise to a quasi-continuum of modes. In combination with spatial hole burning and asymmetric gain/amplification within the arms, this is manifested as dense yet highly irregular THz emission spectra in free-running devices. However, this also makes these devices very suitable for microwave modulation experiments. Most notably, we demonstrated actively mode-locked coherent pulse trains with pulse widths down to 2.3 ps, which is the shortest pulse duration for any THz QCL to date. Additionally, mode-locked pulses with very clean shapes and smooth spectral envelopes spanning a bandwidth of 700 GHz were measured. Such coherent mode-locked pulses with short durations and wide emission bandwidths are interesting for use both in fundamental studies, e.g., using THz field-induced excitations, as well as for practical applications, such as imaging and spectroscopy.

ACKNOWLEDGMENTS

The authors gratefully acknowledge funding from the ERC Grant CHIC (Grant No. 724344) and SNF grant 200021-232335. This work was part of the 23FUN04 COMOMET project that has received funding from the European Partnership on Metrology, co-financed from the European Union's Horizon Europe Research and Innovation Programme and by the Participating States, Funder ID 10.13039/100019599.

DATA AVAILABILITY

The data that support the findings of this study are available within the article and its supplementary material.

REFERENCES

- ¹C.-J. Yang, J. Li, M. Fiebig, and S. Pal, "Terahertz control of many-body dynamics in quantum materials," *Nature Reviews Materials* **8**, 518–532 (2023).
- ²D. Nicoletti and A. Cavalleri, "Nonlinear light–matter interaction at terahertz frequencies," *Adv. Opt. Photon.* **8**, 401–464 (2016).
- ³D. Alves-Lima, J. Song, X. Li, A. Portieri, Y. Shen, J. A. Zeitler, and H. Lin, "Review of terahertz pulsed imaging for pharmaceutical film coating analysis," *Sensors* **20**, 1441 (2020).
- ⁴R. J. B. Dietz, N. Vieweg, T. Puppe, A. Zach, B. Globisch, T. Göbel, P. Leisching, and M. Schell, "All fiber-coupled THz-TDS system with kHz measurement rate based on electronically controlled optical sampling," *Opt. Lett.* **39**, 6482–6485 (2014).
- ⁵J. Faist, F. Capasso, D. L. Sivco, C. Sirtori, A. L. Hutchinson, and A. Y. Cho, "Quantum cascade laser," *Science* **264**, 553–556 (1994).
- ⁶G. Scalari and J. Faist, "30 years of the quantum cascade laser," *Communications Physics* **7**, 394 (2024).
- ⁷S. Barbieri, M. Ravarro, P. Gellie, G. Santarelli, C. Manquest, C. Sirtori, S. P. Khanna, E. H. Linfield, and A. G. Davies, "Coherent sampling of active mode-locked terahertz quantum cascade lasers and frequency synthesis," *Nature Photonics* **5**, 378–378 (2011).
- ⁸A. Hugi, G. Villares, S. Blaser, H. C. Liu, and J. Faist, "Mid-infrared frequency comb based on a quantum cascade laser," *Nature* **492**, 229–233 (2012).
- ⁹U. Senica, A. Dikopoltsev, A. Forrer, S. Cibella, G. Torrioli, M. Beck, J. Faist, and G. Scalari, "Frequency-modulated combs via field-enhancing tapered waveguides," *Laser & Photonics Reviews* **17**, 2300472 (2023).
- ¹⁰B. Meng, M. Singleton, J. Hillbrand, M. Francké, M. Beck, and J. Faist, "Dissipative Kerr solitons in semiconductor ring lasers," *Nature Photonics* **16**, 142–147 (2022).
- ¹¹N. Opačak, D. Kazakov, L. L. Columbo, M. Beiser, T. P. Letsou, F. Pilat, M. Brambilla, F. Prati, M. Piccardo, F. Capasso, *et al.*, "Nozaki–Bekki solitons in semiconductor lasers," *Nature* **625**, 685–690 (2024).
- ¹²P. Micheletti, U. Senica, A. Forrer, S. Cibella, G. Torrioli, M. Francké, M. Beck, J. Faist, and G. Scalari, "Terahertz optical solitons from dispersion-compensated antenna-coupled planarized ring quantum cascade lasers," *Science Advances* **9**, eadf942 (2023).
- ¹³I. Heckelmann, M. Bertrand, A. Dikopoltsev, M. Beck, G. Scalari, and J. Faist, "Quantum walk comb in a fast gain laser," *Science* **382**, 434–438 (2023).
- ¹⁴R. Köhler, A. Tredicucci, F. Beltram, H. E. Beere, E. H. Linfield, A. G. Davies, D. A. Ritchie, R. C. Iotti, and F. Rossi, "Terahertz semiconductor-heterostructure laser," *Nature* **417**, 156–159 (2002).
- ¹⁵G. Scalari, C. Walther, M. Fischer, R. Terazzi, H. Beere, D. Ritchie, and J. Faist, "THz and sub-THz quantum cascade lasers," *Laser & Photonics Reviews* **3**, 45–66 (2009).
- ¹⁶M. Shahili, S. J. Addamane, A. D. Kim, C. A. Curwen, J. H. Kawamura, and B. S. Williams, "Continuous-wave GaAs/AlGaAs quantum cascade laser at 5.7 THz," *Nanophotonics* **13**, 1735–1743 (2024).
- ¹⁷A. Khalatpour, A. K. Paulsen, C. Deimert, Z. R. Wasilewski, and Q. Hu, "High-power portable terahertz laser systems," *Nature Photonics* **15**, 16–20 (2021).
- ¹⁸S. Gloor, A. Weisenhorn, L. Hetier, U. Senica, R. Maulini, M. Beck, J. Faist, and G. Scalari, "Compact, thermoelectrically cooled surface emitting THz QCLs operating in an HHL housing," *Nanophotonics* **14**, 3415–3421 (2025).
- ¹⁹B. S. Williams, "Terahertz quantum-cascade lasers," *Nature Photonics* **1**, 517–525 (2007).
- ²⁰U. Senica, A. Forrer, T. Olariu, P. Micheletti, S. Cibella, G. Torrioli, M. Beck, J. Faist, and G. Scalari, "Planarized THz quantum cascade lasers for broadband coherent photonics," *Light: Science & Applications* **11**, 347 (2022).
- ²¹M. Rösch, G. Scalari, M. Beck, and J. Faist, "Octave-spanning semiconductor laser," *Nature Photonics* **9**, 42–47 (2015).
- ²²D. Burghoff, T.-Y. Kao, N. Han, C. W. I. Chan, X. Cai, Y. Yang, D. J. Hayton, J.-R. Gao, J. L. Reno, and Q. Hu, "Terahertz laser frequency combs," *Nature Photonics* **8**, 462–467 (2014).
- ²³M. Rösch, G. Scalari, M. Beck, and J. Faist, "Octave-spanning semiconductor laser," *Nat. Photonics* **9**, 42–47 (2015).
- ²⁴K. Garrasi, F. P. Mezzapesa, L. Salemi, L. Li, L. Consolino, S. Bartalini, P. De Natale, A. G. Davies, E. H. Linfield, and M. S. Vitiello, "High Dynamic Range, Heterogeneous, Terahertz Quantum Cascade Lasers Featuring Thermally Tunable Frequency Comb Operation over a Broad Current Range," *ACS Photonics* **6**, 73–78 (2019).
- ²⁵A. Mottaghizadeh, D. Gacemi, P. Laffaille, H. Li, M. Amanti, C. Sirtori, G. Santarelli, W. Hänsel, R. Holzwart, L. H. Li, E. H. Linfield, and S. Barbieri, "5-ps-long terahertz pulses from an active-mode-locked quantum cascade laser," *Optica* **4**, 168–171 (2017), publisher: Optical Society of America.
- ²⁶L. K. Hoffmann, C. A. Hurni, S. Schartner, M. Austerer, E. Mujagic, M. Nobile, A. Benz, W. Schrenk, A. M. Andrews, P. Klang, and G. Strasser, "Coherence in Y-coupled quantum cascade lasers," *Applied Physics Letters* **91**, 161106 (2007).
- ²⁷O. P. Marshall, S. Chakraborty, M. Khairuzzaman, H. E. Beere, and D. A. Ritchie, "Reversible mode switching in Y-coupled terahertz lasers," *Applied Physics Letters* **102**, 111105 (2013).
- ²⁸I. Kundu, P. Dean, A. Valavanis, J. R. Freeman, M. C. Rosamond, L. Li, Y. Han, E. H. Linfield, and A. G. Davies, "Continuous frequency tuning with near constant output power in coupled Y-branched terahertz quantum cascade lasers with photonic lattice," *ACS Photonics* **5**, 2912–2920 (2018).
- ²⁹A. Forrer, M. Francké, D. Stark, T. Olariu, M. Beck, J. Faist, and G. Scalari, "Photon-driven broadband emission and frequency comb RF injection locking in THz quantum cascade lasers," *ACS Photonics* **7**, 784–791 (2020).

³⁰S. Molesky, Z. Lin, A. Y. Piggott, W. Jin, J. Vucković, and A. W. Rodriguez, “Inverse design in nanophotonics,” *Nature Photonics* **12**, 659–670 (2018).

³¹U. Senica, S. Gloor, P. Micheletti, D. Stark, M. Beck, J. Faist, and G. Scalari, “Broadband surface-emitting THz laser frequency combs with inverse-designed integrated reflectors,” *APL Photonics* **8**, 096101 (2023).

³²V. Digiorgio, U. Senica, P. Micheletti, M. Beck, J. Faist, and G. Scalari, “On-chip, inverse-designed active wavelength division multiplexer at THz frequencies,” *Nature Communications* **16**, 7711 (2025).

³³D. S. Wiersma, “The physics and applications of random lasers,” *Nature Physics* **4**, 359–367 (2008).

³⁴Z. Han, D. Ren, and D. Burghoff, “Sensitivity of SWIFT spectroscopy,” *Optics Express* **28**, 6002–6017 (2020).

³⁵G. Torrioli, A. Forrer, M. Beck, P. Carelli, F. Chiarello, J. Faist, A. Gaggero, E. Giovine, F. Martini, U. Senica, *et al.*, “THz optical beat-note detection with a fast superconducting hot electron bolometer operating up to 31 GHz,” *Optics Express* **31**, 15942–15952 (2023).

³⁶F. Wang, H. Nong, T. Fobbe, V. Pistore, S. Houver, S. Markmann, N. Jukam, M. Amanti, C. Sirtori, S. Moumdji, *et al.*, “Short terahertz pulse generation from a dispersion compensated modelocked semiconductor laser,” *Laser & Photonics Reviews* **11**, 1700013 (2017).

³⁷E. Riccardi, V. Pistore, S. Kang, L. Seitner, A. De Vetter, C. Jirauschek, J. Mangeney, L. Li, A. G. Davies, E. H. Linfield, *et al.*, “Short pulse generation from a graphene-coupled passively mode-locked terahertz laser,” *Nature Photonics* **17**, 607–614 (2023).

³⁸T. J. Kippenberg, A. L. Gaeta, M. Lipson, and M. L. Gorodetsky, “Dissipative Kerr solitons in optical microresonators,” *Science* **361**, eaan8083 (2018).

³⁹U. Senica, M. A. Schreiber, P. Micheletti, M. Beck, C. Jirauschek, J. Faist, and G. Scalari, “Continuously tunable coherent pulse generation in semiconductor lasers,” *arXiv preprint arXiv:2411.11210* (2024).

⁴⁰L. K. Hoffmann, M. Klinkmüller, E. Mujagić, M. P. Semtsiv, W. Schrenk, W. T. Masselink, and G. Strasser, “Tree array quantum cascade laser,” *Optics express* **17**, 649–657 (2009).

Supplementary Material for Short mode-locked pulses from planarized Y-coupled THz lasers

U. Senica,^{1, 2, a)} T. Bühler,^{1, 3} S. Cibella,⁴ G. Torrioli,⁴ M. Beck,¹ J. Faist,¹ and G. Scalari^{1, b)}

¹⁾*Quantum Optoelectronics Group, Institute of Quantum Electronics, ETH Zürich, 8093 Zürich, Switzerland*

²⁾*John A. Paulson School of Engineering and Applied Sciences, Harvard University, 02138 Cambridge, USA*

³⁾*Institute of Physics and Center for Quantum Science and Engineering, Ecole Polytechnique Fédérale de Lausanne, CH-1015 Lausanne, Switzerland*

⁴⁾*Istituto di Fotonica e Nanotecnologie, CNR, Via del Fosso del Cavaliere 100, 00133 Rome, Italy*

(Dated: 10 February 2026)

I. INVERSE-DESIGNED Y-SPLITTERS

The Y-splitter regions were obtained using the `lumopt` inverse design Python package within the Ansys/Lumerical FDTD simulation software. In particular, we modeled the device using a 2.5D simulation of the wave propagation along a central slice of the device. This is feasible due to the planarized waveguide geometry, where the field distribution is nearly constant along the vertical direction, as the waveguiding structure is sandwiched between two metallic sheets. Additionally, due to symmetry, only half of the device could be simulated, further reducing the computational load. The Y-splitter region was obtained via shape optimization, where the outline was defined with several control points that were connected using a smooth interpolating spline. Employing the adjoint optimization approach, the fundamental TM mode was launched into the single waveguide, and the modal transmission into one of the arms was measured. Combining the results of a direct (forward) and adjoint (backwards) simulation gives the gradient field, which is used to update the shape of the Y-splitter region, improving its performance in the next iteration.

A detailed view of the optimization run and the evolution of various geometrical and optimization parameters is shown in Fig. S1, where convergence is reached after 250 iterations. Due to the reduced dimensionality (2.5D), use of spatial symmetry, and the fast convergence of adjoint optimization, this only takes a few hours on a normal desktop computer. We designed two generations of devices, where the Figure of Merit (FOM) was to maximize equal (50:50) transmission into each of the arms over an octave-spanning bandwidth between 2-4 THz. The simulated performance is shown in Fig. S2, where both the first- and second-generation devices show a similar performance, close to the target transmission. Y-splitter 1 splits a 20 μm wide input waveguide into two 20 μm arms, while Y-splitter 2 uses a 40 μm wide input waveguide.

II. ADDITIONAL EXPERIMENTAL RESULTS

In this section, we present additional experimental results from several devices.

The first-generation Y-coupled device has relatively narrow waveguide widths of 20 μm , resulting in a small active area and a relatively low threshold current of 60 mA, as shown in the measured LIV curve in Fig. S3. The measurement was done in pulsed mode at a duty cycle of 10%, reaching a peak power of around 0.5 mW. In contrast, the second-generation Y-coupled device has wider waveguide widths of 40 μm with a larger active area, lower waveguide losses, and higher gain, resulting in a wider dynamic range and increased output power.

The symmetric device has a wide range of bias voltages where a single RF beatnote is measured, as can be seen in Fig. S4. This is in stark contrast to the seemingly chaotic beatnote map of the asymmetric device (main text, Fig. 3a), and indicates that the device is indeed fully symmetric, producing a single beatnote that is typical for coherent comb states, as often observed in Fabry-Pérot QCLs.

In Fig. S5, we show the measured far-field pattern of a second-generation Y-coupled device with symmetric arms, where we again observe a very clear interference pattern in the horizontal direction. Here, the sample was mounted at the very edge of the copper submount, so there are no reflections and additional interference effects in the vertical direction.

III. ANALYTICAL CALCULATIONS OF FAR-FIELD PATTERNS

We developed an analytical model to calculate the predicted far-field patterns of the Y-coupled device. In the simplest case, this is analogous to a double-slit experiment with two spatially separated sources. The following formula can be used for computing the far-field intensity in the horizontal direction^{1,2}:

$$I(\varphi) \propto \cos^2\left(\frac{\pi\Delta\sin(\varphi)}{\lambda}\right) \cdot \text{sinc}^2\left(\frac{\sin(\varphi)a_x}{\lambda}\right) \cdot \cos^2(\varphi) \quad (1)$$

where φ is the emission angle, Δ the distance between the two slits (between the two waveguide centers), a_x is the width of the slit, and λ is the emission wavelength, where in our case, the dominant contribution comes from the $\cos^2\left(\frac{\pi\Delta\sin(\varphi)}{\lambda}\right)$ term. To get the total intensity, we sum the intensity pattern of each measured frequency in the emission spectrum, normalized and weighted by its relative intensity. In Eq. 1, we assumed that the electric field of the emitted light from the two Y-splitter arms is equal in amplitude and in phase (i.e., the two

^{a)}usenica@seas.harvard.edu

^{b)}scalari@phys.ethz.ch

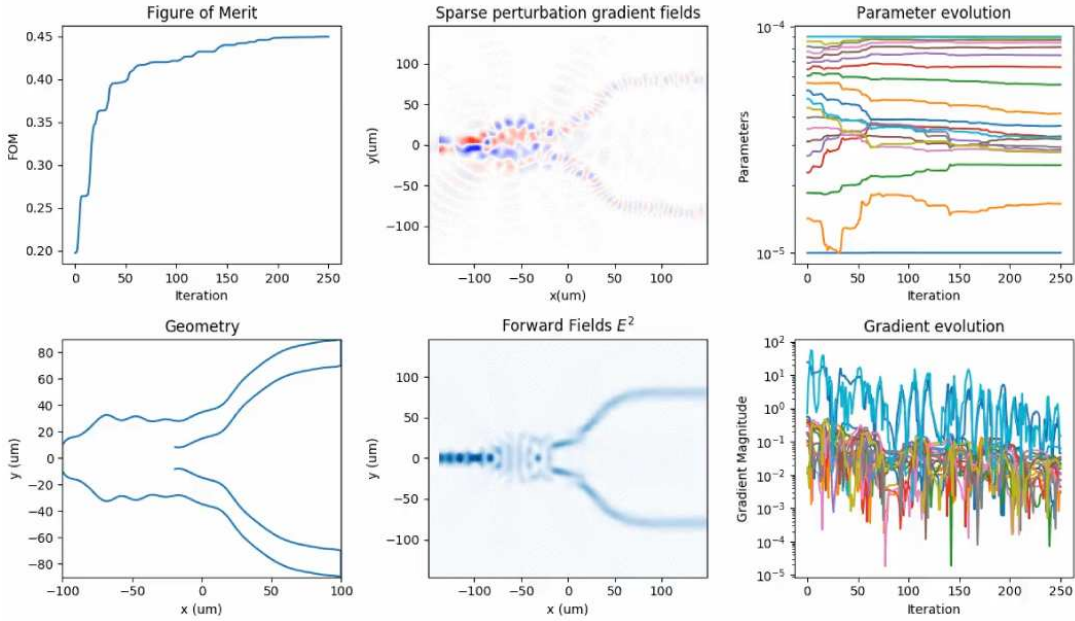


FIG. S1. Snapshot of the inverse design optimization run of the first-generation Y-splitter, displaying the various geometric and optimization parameters, converging after 250 iterations.

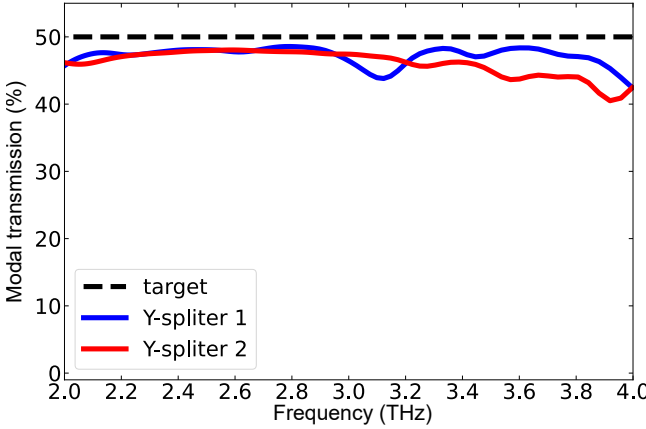


FIG. S2. Computed fundamental mode transmission of the optimized Y-splitter structure into one of the arms over an octave-spanning frequency range between 2-4 THz. Both generations of devices show a similar performance, close to the target transmission of 50% over the bandwidth of interest (50:50 splitting ratio).

arms are phase-locked). We can also include additional terms for more general cases. If there is a relative phase shift, we can write:

$$I(\varphi) \propto \left| e^{i\gamma} \cdot e^{\frac{i\pi\Delta\sin(\varphi)}{\lambda}} + e^{\frac{-i\pi\Delta\sin(\varphi)}{\lambda}} \right|^2 \cdot \text{sinc}^2\left(\frac{\sin(\varphi)a_x}{\lambda}\right) \cdot \cos^2(\varphi) \quad (2)$$

where γ is the relative phase shift between the two arms. As can be seen in Fig. S6, the multi-lobed interference pattern is centered if the arms are in phase, and off-center for increasing

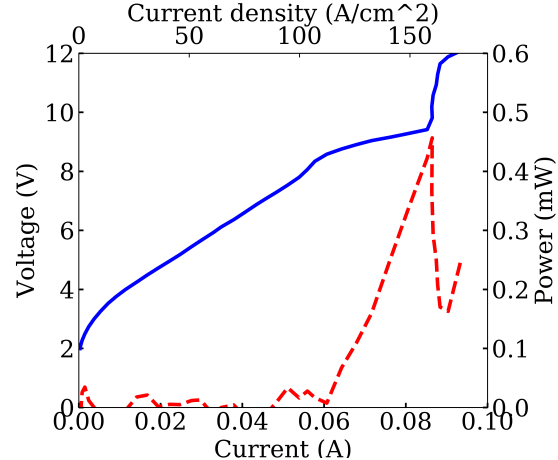


FIG. S3. Measured LIV curve of the symmetric Y-coupled device, displaying a low threshold current of 60 mA.

phase shifts. At $\gamma = 180^\circ$, there is a local minimum in the central direction.

If instead, there is a difference in amplitude between the two arms, we can write:

$$I(\varphi) \propto \left| \lambda_1 \cdot e^{\frac{i\pi\Delta\sin(\varphi)}{\lambda}} + \lambda_2 \cdot e^{\frac{-i\pi\Delta\sin(\varphi)}{\lambda}} \right|^2 \cdot \text{sinc}^2\left(\frac{\sin(\varphi)a_x}{\lambda}\right) \cdot \cos^2(\varphi) \quad (3)$$

where λ_1 and λ_2 are real numbers that determine the amplitudes of the individual arms with $0 \leq (\lambda_1, \lambda_2) \leq 1$ and $\lambda_1^2 + \lambda_2^2 = 1$. As shown in Fig. S7, with increasingly different power splitting ratios of the two arms, the contrast of the

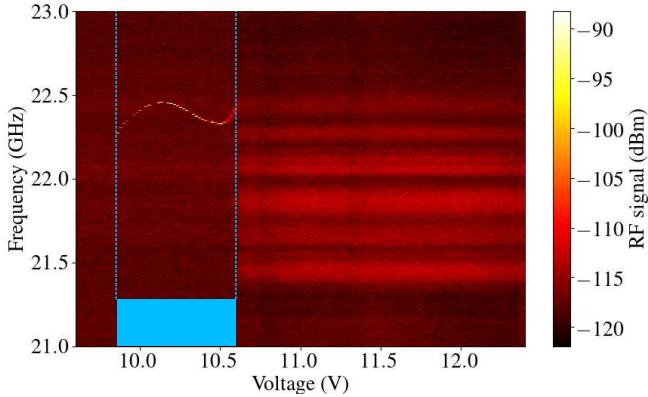


FIG. S4. Measured RF beat note map for the symmetric Y-coupled device, displaying a wide region of low bias voltages with a single RF beat note, an indication of frequency comb operation.

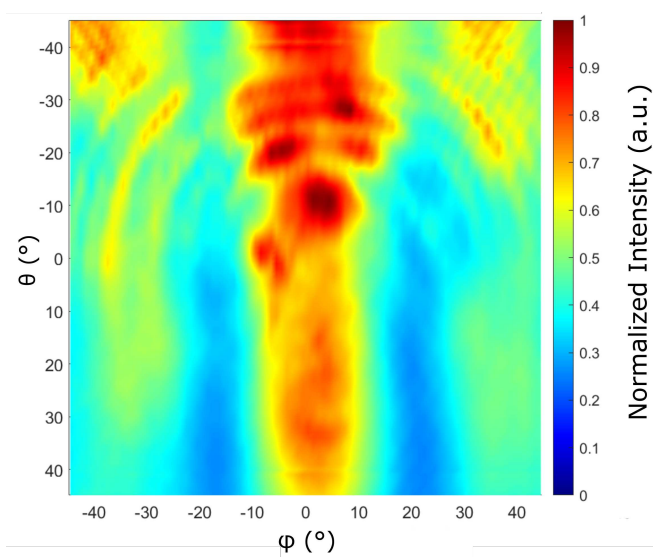


FIG. S5. Measured far-field pattern of a second-generation device with symmetric arms, showing clear interference lines.

far-field interference pattern is significantly reduced. As the total integrated curve intensities (i.e., total emission power) are normalized to the same value, the intensities of the individual lobes are gradually reduced, eventually converging to the single waveguide case with a single lobe across the entire range of angles ϕ .

Since our experimentally measured far-field patterns are symmetric, centered at $\phi = 0^\circ$, and feature a strong contrast between the local maxima and minima, we can conclude that the two arms of symmetric Y-coupled devices are in fact emitting light of the same intensity and phase throughout the entire emission spectrum. In other words, they indeed perform well as broadband 50:50 power splitters, as designed.

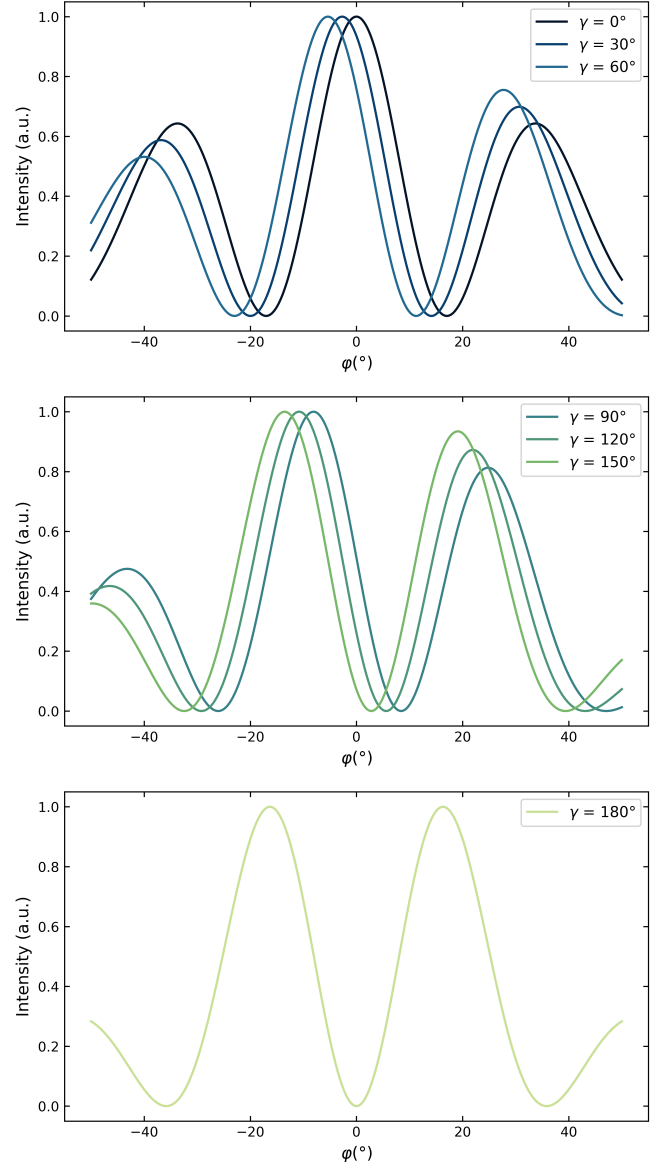


FIG. S6. Analytical 1D calculations of the far-field pattern along a horizontal cross-section as a function of the phase shift between the two arms. The intensities are equal in both arms. Independent phase control could be useful for beam steering applications.

IV. FULL-WAVE 3D SIMULATIONS OF Y-COUPLED DEVICES

To investigate the behavior of asymmetric Y-coupled devices, we performed a series of full-wave 3D electromagnetic simulations using the CST Microwave Studio simulation environment.

With 3D eigenmode/eigenfrequency analysis, we can determine the resonant modes and their corresponding frequencies, in this case searching for 50 eigenmodes above a frequency of 2.98 THz. As shown in Fig. S8, in the case of a symmetric Y-coupled device, we get a standing wave pattern along the entire device oscillating in phase, as typically observed

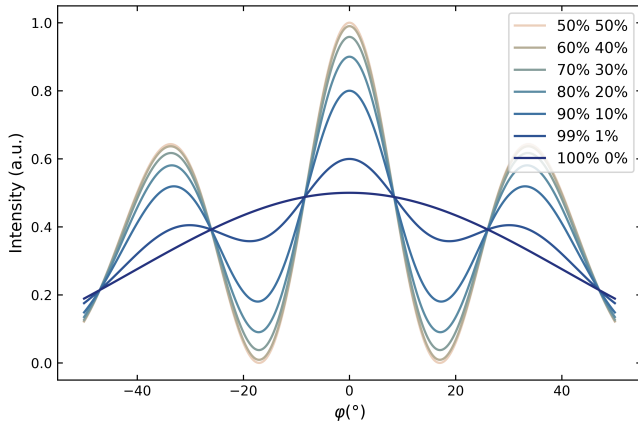


FIG. S7. Analytical 1D calculations of the far-field pattern along a horizontal cross-section as a function of the Y-splitter power ratio. The phase is equal in both arms, and the total intensity is normalized.

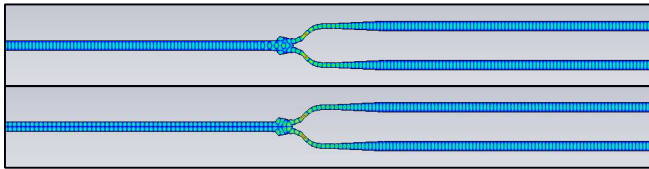


FIG. S8. 3D eigenmode simulations of the symmetric Y-coupled device produce the expected standing wave modes with intensity distributed along the entire waveguide and oscillating in phase, as expected for Fabry-Pérot lasers.

in Fabry-Pérot cavity lasers with finite mirror reflectivities. In contrast, when modeling an asymmetric Y-coupled device, much more complex eigenmodes and field patterns emerge due to the phase delay induced by the asymmetric arms (either due to different arm widths or lengths, respectively). In particular, we can categorize the solutions into three families, depending on the field intensity distribution within the individual arms. As shown in Fig. S9, there are eigenmodes with intensity distributed along all three arms ($N = 3$). However, the device asymmetry and the induced phase delay need to be compensated for such a mode to be supported, typically by wiggly oscillations or higher-order transversal modes in the main waveguide. These kinds of modes appear less often in the eigenmode analysis. Instead, the most common are eigenmodes with significant field intensity in the main waveguide and in one of the arms of the Y-splitter ($N = 2$), as if the two opposite arms would combine into a single Fabry-Pérot cavity. Additionally, eigenmodes with significant intensity in only one of the arms are also observed ($N = 1$). In this case, higher-order transverse modes within the arm are reflected when approaching the Y-splitter region due to the waveguide narrowing. When considering the simulated eigenfrequencies of these modes, we find regions with very high mode densities, e.g., 20 eigenmodes lie within a frequency band of less than 20 GHz. This average mode spacing of less than 1 GHz is much smaller than the usual FSR of a 2.7 mm long Fabry-Pérot planarized waveguide of around 15 GHz. We

also ran eigenmode simulations at RF frequencies, relevant for RF beatnote readout and RF injection of external signals. As expected, these eigenmodes are nearly uniform across the extended metallization (2D waveguide cross-section), and make up multilobed standing waves along the entire device length, very similar to standard planarized waveguides³. This is because the top and bottom metallic electrodes dominate the microwave properties of the waveguide, regardless of the non-uniform distribution of active material and BCB. Therefore, the Y-coupled active waveguide shape does not play a significant role at RF frequencies.

Additionally, we performed wave propagation simulations, in which a fundamental mode source at a specific frequency is launched from the main waveguide facet, allowing us to visualize the spatiotemporal evolution of the optical field within the cavity. In Fig. S10, we show snapshots of the electric field within a central slice along the asymmetric device with different arm widths for several values of the optical phase, i.e., different moments in time. We can see that a complex field pattern emerges, with wiggly oscillations within the main waveguide and a phase delay between the maximum intensities between the Y-splitter arms.

Based on these results of the 3D eigenmode and time-domain simulations of the asymmetric Y-coupled cavity, we can draw some conclusions. First of all, the asymmetry, phase delay, and waveguide narrowing give rise to a large number of eigenmodes within a narrow frequency band, resulting in a very high density of modes. Secondly, in the time domain, there are complex field patterns and dynamics, such as wiggly oscillations and delays (breathing) between the individual arms. Additionally, in an active laser device (not taken into account in such simulations), there is a significant spatial hole burning effect that favors multi-mode operation. On top of that, the different arm widths or lengths result in a different gain/amplification factor, such that the inputs to the Y-splitter are no longer the same amplitude and/or phase, which can modify the splitting ratio as a function of frequency and laser bias. Therefore, in free-running devices, these effects result in a large number of simultaneously lasing modes with uneven spacing, as seen from the seemingly chaotic RF beatnote maps and uneven emission spectrum (see also Main Text, Fig. 3). However, in RF-modulated devices, this facilitates the generation of spectra with tunable mode spacings (repetition rates), as there is a quasi-continuum of eigenmodes that can be selectively excited. Similarly, when biased close to the lasing threshold and RF-modulated close to the quasi-resonant repetition rate, we are able to generate very broadband coherent trains of short pulses. This is different from active mode-locking of Fabry-Pérot lasers, as the resonant excitation is limited to a discrete set of longitudinal modes, resulting in a narrower obtainable bandwidth and longer pulse durations due to chromatic dispersion.

V. TUNABLE MODE SPACING

In this section, we investigate emission spectra with a continuously tunable mode spacing (Main Text, Fig. 5), similar to

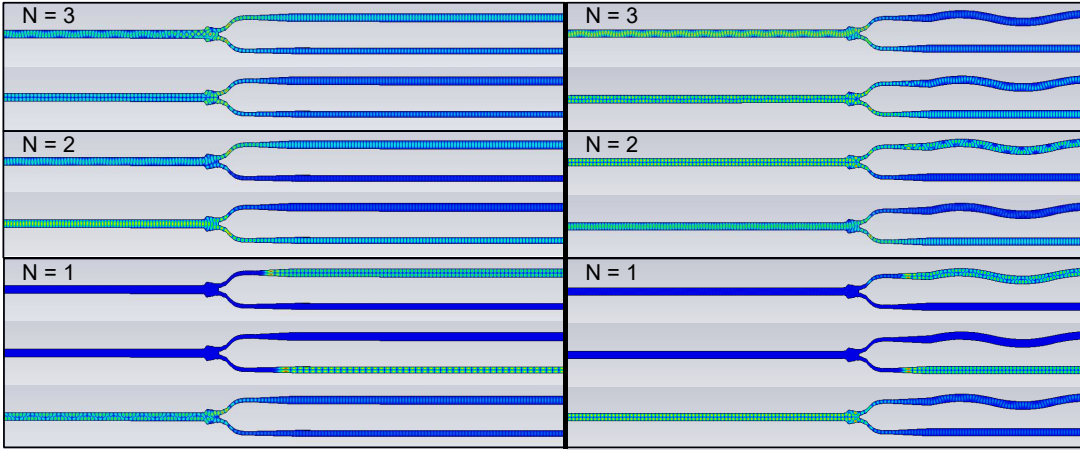


FIG. S9. 3D eigenmode simulations of both asymmetric Y-coupled devices, categorized into different mode families based on the intracavity field intensity distribution.

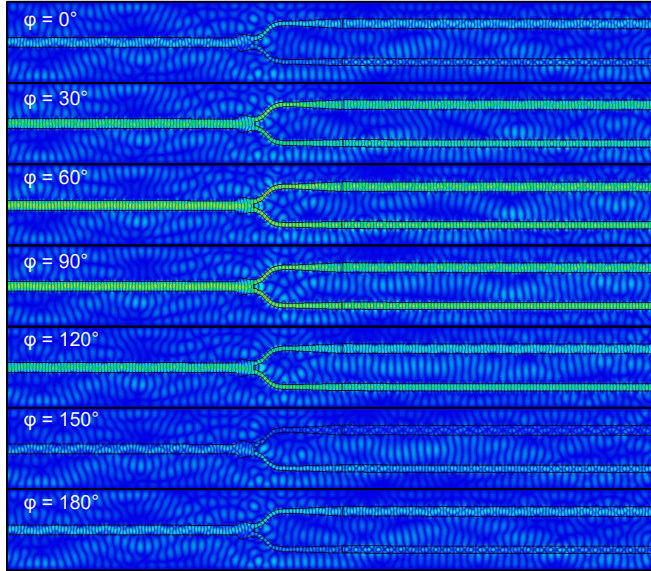


FIG. S10. 3D wave propagation simulation of a full asymmetric Y-coupled device: the fundamental waveguide mode is launched from the left port (single waveguide) and the steady-state field intensity is observed. In the images, we show the electric field intensity at a frequency of 3.1 THz at different values of the optical phase ϕ . Several interesting properties are revealed: the two arms are slightly out of phase, and the field sometimes has a “twisted” shape, which indicates multi-mode operation (or mode conversion).

our recent work⁴. When sweeping the RF injection frequency, a variety of different states are observed. These have characteristic shapes, appearing throughout the spectrum, and can be categorized into different families. In Fig. S11, we display examples of different types of states. On the left side, we show the measured emission spectra, while on the right, we add a simulated spectrum, which is based on a simple sideband calculation. Specifically, in the simple model, we can (arbitrarily) define a set of initial lasing modes in the spectrum (blue lines), which act as seed modes for the RF injection. In partic-

ular, a cascade of coherent sidebands (red lines) is generated with a spacing equal to the RF injection frequency, with a decreasing intensity further away from the corresponding seed mode. Additionally, we also added the blue envelope function, which represents the reconstructed spectrum with the actual measurement resolution of 0.075 cm^{-1} .

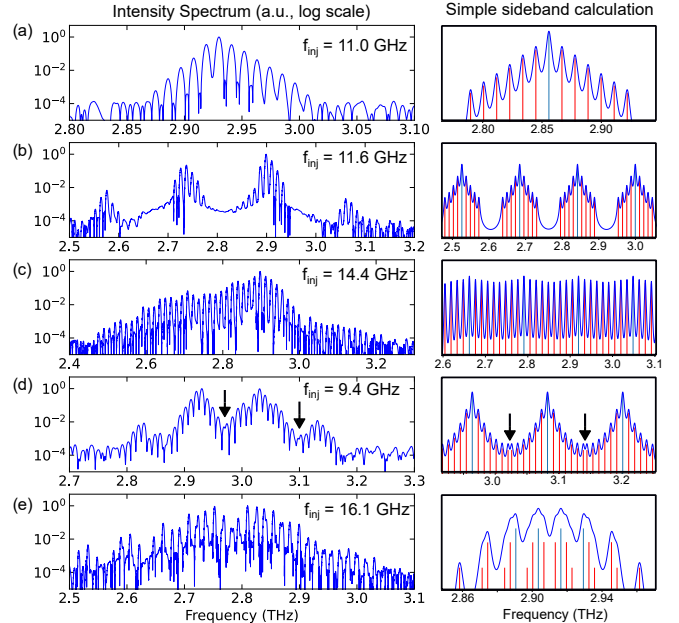


FIG. S11. A zoo of RF-generated states, where we show different families of measured emission spectra along with a simple sideband calculation, where the seed lasing modes (blue) generate coherent sidebands (red), and the spectral envelope is computed to simulate the measured spectrum envelope with a limited spectral resolution. Details on each type of state are provided in the text.

Using the experimental data and the analytical model, we can describe each mode family.

(a) Sometimes, a single-lobed spectrum around a central maximum mode is observed, typically consisting of 10-20

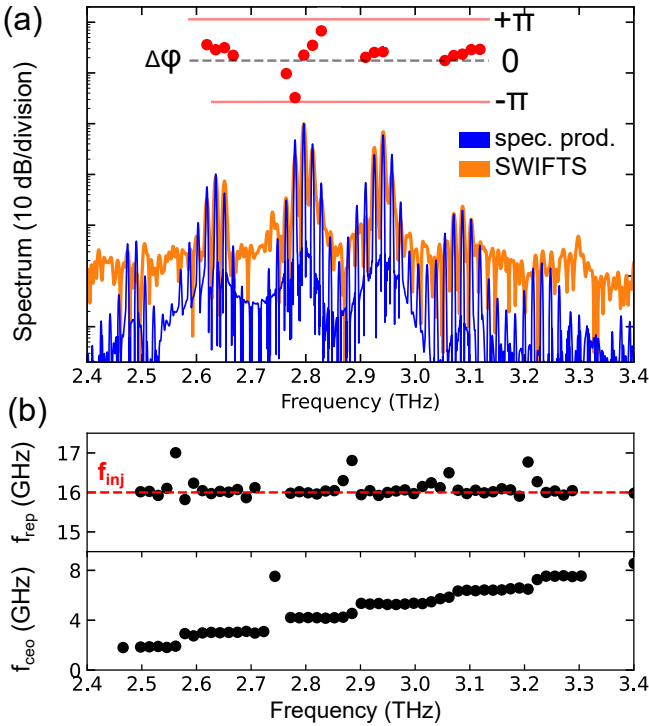


FIG. S12. SWIFT spectroscopy of a broadband multi-lobed state with an injection frequency of 16 GHz.

modes. This can easily be reproduced with a single central lasing (seed) mode and a cascade of coherent sidebands generated by the RF on each side, which is also similar to the usual active mode-locking results obtained on ridge waveguide samples close to the laser threshold. This is the basic “building block” that is used in composing more complex spectra with the simple model.

(b) More often, several such lobes are observed throughout the emission spectrum, which can be reproduced as sparse lasing (seed) modes with coherent sidebands that populate the proximity of each seed mode. Sometimes, these are well separated with spectral gaps in between.

(c) Continuous spectra are also observed quite often at various injection frequencies. This is not at all limited to the proximity of the free-running mode spacing: if there is an integer number of sidebands that fit between the seed lasing modes, a continuous spectrum can be produced. This could potentially

lead to the generation of fractional harmonic combs.

(d) In some cases, double modes can be observed at the boundaries between two spectral lobes (indicated by arrows). These stitching points appear when the cascade of coherent sidebands generated by two neighbouring seed modes propagates far enough, but an integer number of sidebands does not fit between the two seed modes. In this case, a discontinuity in the mode spacing can be observed as a stitching point in the spectrum.

(e) At injection frequencies slightly above the free-running mode spacing, broadened or double modes can be observed in the spectrum. With the proximity of the free-running mode spacing, the most likely explanation is that both the fundamental longitudinal modes and the coherent sidebands are excited simultaneously. The sideband modes are positioned close to the lasing modes, but generated from another neighboring lasing mode. The sideband calculation shows a simplified example with only a few modes. We should note that with a further increase of the RF injection frequency (above around 16.5 GHz), the mode spacing again starts to follow precisely the injection frequency.

Finally, we also investigated one of the broadband multi-lobed states with SWIFT spectroscopy. As expected, each of the individual lobes is coherent, with the injected mode spacing of 16 GHz (since there are spectral gaps between the lobes, the time-domain signal cannot be reconstructed). A simple analysis of f_{rep} and f_{ceo} in panel (b) shows that, while the mode spacing within each lobe follows the RF drive frequency, the offset within each lobe is different, as indicated by the staircase shape in the plot. This means that a series of sub-combs is formed, and the stitching points that are sometimes observed in fact result from a shift of the f_{ceo} .

VI. REFERENCES

- ¹E. Hecht, *Optics* (Addison-Wesley Publishing Company, 1987).
- ²M. Born and E. Wolf, *Principles of optics: electromagnetic theory of propagation, interference and diffraction of light* (Elsevier, 2013).
- ³U. Senica, A. Forrer, T. Olariu, P. Micheletti, S. Cibella, G. Torrioli, M. Beck, J. Faist, and G. Scalari, “Planarized THz quantum cascade lasers for broadband coherent photonics,” *Light: Science & Applications* **11**, 347 (2022).
- ⁴U. Senica, M. A. Schreiber, P. Micheletti, M. Beck, C. Jirauschek, J. Faist, and G. Scalari, “Continuously tunable coherent pulse generation in semiconductor lasers,” arXiv preprint arXiv:2411.11210 (2024).